Available online at www.sciencedirect.com
SCIENCE DIRECT®
Biochemical and Biophysical Research Communications 338 (2005) 206–214
BBRC
www.elsevier.com/locate/ybbrc

Spectroscopic and computational studies of NTBC bound to the non-heme iron enzyme (4-hydroxyphenyl)pyruvate dioxygenase: Active site contributions to drug inhibition

Michael L. Neidig [a], Andrea Decker [a], Michael Kavana [b], Graham R. Moran [b,*], Edward I. Solomon [a,*]

[a] Department of Chemistry, Stanford University, Stanford, CA 94305, USA
[b] Department of Chemistry and Biochemistry, University of Wisconsin—Milwaukee, Milwaukee, WI 53211, USA

Received 16 July 2005
Available online 9 September 2005

Abstract

(4-Hydroxyphenyl)pyruvate dioxygenase (HPPD) is an α-keto-acid-dependent dioxygenase which catalyzes the conversion of (4-hydroxyphenyl)pyruvate (HPP) to homogentisate as part of tyrosine catabolism. While several di- and tri-ketone alkaloids are known as inhibitors of HPPD and used commercially as herbicides, one such inhibitor, [2-nitro-4-(trifluoromethyl)benzoyl]-1,3-cyclohexanedione (NTBC), has also been used therapeutically to treat type I tyrosinemia and alkaptonuria in humans. To gain further insight into the mechanism of inhibition by NTBC, a combination of CD/MCD spectroscopy and DFT calculations of HPPD/Fe^{II}/NTBC has been performed to evaluate the contribution of the Fe^{II}–NTBC bonding interaction to the high affinity of this drug for the enzyme. The results indicate that the bonding of NTBC to Fe^{II} is very similar to that for HPP, both involving similar π-backbonding interactions between NTBC/HPP and Fe^{II}. Combined with the result that the calculated binding energy of NTBC is, in fact, ~3 kcal/mol less than that for HPP, the bidentate coordination of NTBC to Fe^{II} is not solely responsible for its extremely high affinity for the enzyme. Thus, the π-stacking interactions between the aromatic rings of NTBC and two phenyalanine residues, as observed in the crystallography of the HPPD/Fe^{II}/NTBC complex, appear to be responsible for the observed high affinity of drug binding.

Keywords: Non-heme iron; Structure-activity relationships; α-Ketoglutarate dioxygenases; Drug inhibition; (4-Hydroxyphenyl)pyruvate dioxygenase; Magnetic circular dichroism; Density function theory

The α-ketoglutarate (α-KG)-dependent dioxygenases comprise an extensive class of mononuclear non-heme enzymes which require Fe^{II}, α-KG, and dioxygen for catalysis [1]. A sub-class of these enzymes exist which are unique in that both oxygen atoms of dioxygen are incorporated into a single substrate as the α-keto acid moiety is covalently linked to the substrate. (4-hydroxyphenyl)pyruvate dioxygenase (HPPD) is an important member of this sub-class, catalyzing the conversion of the (4-hydroxyphenyl)pyruvate (HPP) to homogentisate as part of tyrosine catabolism (Scheme 1) [2,3].

Di- and tri-ketone alkaloids, produced by a number of myrtaceous plants and lichens to prevent the growth of surrounding plants and/or microbes [4,5], act as selective inhibitors of HPPD [6,7]. Since their discovery, extensive synthetic efforts have been undertaken towards the development of similar compounds [8,9], resulting in selective broad leaf herbicides such as mesotrione and isofluxatole [10,11]. Importantly, another of these inhibitors developed as a herbicide, 2-[2-nitro-4-(trifluoromethyl)benzoyl]-1,3-cyclohexanedione (NTBC), was found to be a successful drug for the treatment of type I tyrosinemia (T1Y), a fatal

* Corresponding authors.
E-mail addresses: moran@uwm.edu (G.R. Moran), edward.solomon@stanford.edu (E.I. Solomon).

0006-291X/$ - see front matter © 2005 Published by Elsevier Inc.
doi:10.1016/j.bbrc.2005.08.242

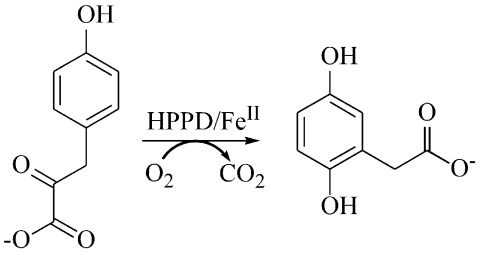

Scheme 1. Conversion of HPP to homogentisate catalyzed by HPPD.

autosomal recessive disease resulting from a defect in the tyrosine catabolism pathway [12]. Since T1Y causes liver cirrhosis, hepatic failure, and an early onset of primary liver cancer [13], the only treatment prior to the development of HPPD inhibitors had been liver transplantation. However, T1Y patients treated with NTBC now are able to live normal lives without the need for liver transplantation. Recently, NTBC has also been used as a successful treatment for alkaptonuria [14], a disease resulting from a deficiency in homogentisate 1,2-dioxygenases which lies downstream of HPPD in the tyrosine catabolism pathway.

While NTBC has been successful as a medical treatment for more than a decade, the mechanism of inhibition is poorly understood. However, recent kinetic and structural studies of the association of NTBC with HPPD have provided key insight into this mechanism. Kinetic studies of the association of NTBC with HPPD demonstrated that it is the exocyclic enol form of the inhibitor which binds exclusively to the ferrous form of the enzyme, yielding a new absorption feature at 450 nm [15]. Using a rapid mixing method, the binding was shown to occur in two phases and comprise three steps, where no pH effects were observed for any of the steps while both of the last two steps exhibited isotope effects. Based on these results, it was proposed that bidentate coordination of the inhibitor precedes Lewis-acid assisted conversion of the bound enol to the enolate. Once formed, the HPPD/Fe^{II}/NTBC complex is unreactive towards dioxygen and bound with a dissociation rate constant essentially equal to zero. Additional insight into the mechanism of inhibition of HPPD by NTBC derives from the crystal structure of the HPPD from *Streptomyces avermitilis* in complex with NTBC at 2.5 Å resolution (Fig. 1) [16]. The structure showed that NTBC is bound bidentately to Fe^{II}, resulting in a predominately five-coordinate ferrous site though a low occupancy water in the sixth coordination position was also observed in one of the protomers. Interestingly, two aromatic residues, Phe364 and Phe336, were observed to sandwich the aromatic ring of NTBC in a π-stacking interaction. While the combination of two distinct binding interactions, bidentate coordination and π-stacking, was proposed to contribute to the extremely high affinity of NTBC for ferrous HPPD, it was not possible to differentiate their individual contributions.

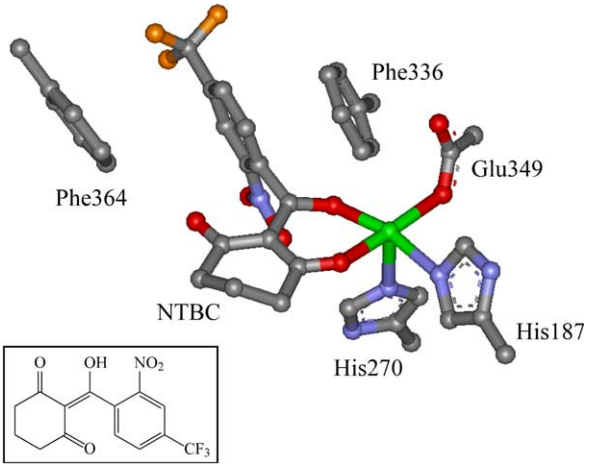

Fig. 1. Active site structure of HPPD/Fe^{II}/NTBC (from PDB 1T47). The inset shows the chemical structure of NTBC in its enol form.

The use of a ferrous methodology employing magnetic circular dichroism (MCD) and variable-temperature variable-field (VTVH) MCD has been successful in elucidating the geometric and electronic structures of the ferrous active sites of mononuclear non-heme iron enzymes, providing molecular level insight into their mechanisms of catalysis [1]. Previously, application of this methodology to the active site geometric and electronic structures of the high-spin $S = 2$ Fe^{II} center in HPPD showed that resting HPPD was a mixture of 6C and 5C species, where the 6C component has a weak axial ligand [17]. This site is relatively stable in the absence of an additional electron donor (i.e., HPP), as the one electron reduction of O_2 is unfavorable due to the low potential and the weak Fe^{3+}–O_2^- that would result [18]. The binding of HPP to resting HPPD results in a new mixture of 6C and 5C species, with bidentate coordination of the α-keto acid moiety of the substrate to Fe^{II} as determined from analysis of the metal-to-ligand charge transfer (MLCT) transitions (at $>15{,}000\ cm^{-1}$) and the $^5T_{2g}$ ground-state splitting determined from the VTVH-MCD data. Unlike resting HPPD, the substrate-bound complex is highly reactive towards O_2 as all the necessary reducing equivalents for oxygen activation are present, enabling catalysis. Thus, despite the fact that HPPD is an α-keto-acid-dependent enzyme, its approach to oxygen activation is similar to those of the extradiol dioxygenases which do not change structure upon binding substrate (5C in both). Overall, the results suggested a resting ferrous active site and approach to oxygen activation by HPPD which bridges those of the α-KG-dependent and extradiol dioxygenases.

In the current study, MCD has been utilized to probe the geometric and electronic structure of the HPPD/Fe^{II}/NTBC complex. Combined with density functional theory (DFT) calculations, the results provide detailed insight into the NTBC–Fe^{II} bonding interactions, including backbonding between Fe^{II} and the inhibitor. Comparison to previous MCD studies and DFT calculations of HPP binding provides a basis for evaluating the individual contribution of

bidentate coordination of NTBC to its high-affinity binding and, hence, its mechanism of drug inhibition.

Experimental

Isolation of HPPD. HPPD was purified according to previously published methods [2]. Unless otherwise stated all enzyme manipulations were undertaken at or below 5 °C. Once isolated the enzyme was concentrated to using centrifugation in a Millipore 10 kDa filter device. The sample was then diluted to ~2 mM in 20 mM Hepes, pH 7.0, and stored at −80 °C.

Preparation of samples for spectroscopy. All commercial reagents were used without further purification: Hepes buffer (Sigma), D_2O (99.9 at. % D, Cambridge Isotope Laboratories), sodium deuteroxide (Sigma), glycerol-d_3 (98 at. % D, Cambridge Isotope Laboratories), and ferrous ammonium sulfate (MCB Manufacturing Chemists, Inc.). NTBC was supplied by Syngenta via Swedish Orphan AB. All samples for spectroscopy were prepared under inert atmosphere inside a N_2-purged wet box. apoHPPD was exchanged into deuterated Hepes buffer (100 mM, pD 7.0) and concentrated to 3.5–4.5 mM using a 4 mL Ultrafree-4 ultrafiltration cell with a 10 kDa membrane. The enzyme was made anaerobic by purging with argon gas on a Schlenk line at 0 °C for 1 h. Fe^{II} and NTBC were added in microliter quantities from anaerobic stock solutions in degassed Hepes buffer (100 mM, pD 7.0). Glycerol-d_3 was added at 50% (v/v) to the HPPD/Fe^{II}/NTBC solution for preparation of MCD samples. CD spectra were taken with and without glycerol addition to ensure that the site was unaffected by the glassing agent. Protein concentrations were determined by measurement of the absorption intensity at $\lambda = 280$ nm with the known extinction coefficient for HPPD ($\varepsilon^{28} = 40.218\ mM^{-1}\ cm^{-1}$). CD and MCD sample concentrations were 2 and 1 mM, respectively.

CD and MCD spectroscopy. Near-IR (600–2000 nm) CD and MCD data were recorded on a Jasco J-200D spectropolarimeter with a liquid N_2-cooled InSb detector and equipped with an Oxford Instruments SM4000-7 Tesla (T) superconducting magnet/cryostat capable of fields up to 7 T and temperatures down to 1.5 K. UV/Vis (300–900 nm) MCD data were recorded on a Jasco J810 spectropolarimeter with an extended S-20 photomultiplier tube and equipped with an Oxford Instruments SM4000-7T superconducting magnet/cryostat capable of fields up to 7 T and temperatures down to 1.5 K.

CD samples were prepared under inert atmosphere in a custom-made 1 cm pathlength masked optical cell (Wilmad) fitted with a gastight Teflon stopcock (LabGlass) and kept at 4 °C during data collection with a circulating cooling bath attached to the sample holder. Low temperature MCD data were obtained in custom-made cells consisting of two Infrasil quartz disks separated by a 0.3 cm thick neoprene O-ring spacer into which the sample was injected and secured between two copper plates.

CD spectra were corrected for buffer and cell baselines by subtraction. MCD spectra were corrected for the natural CD and zero-field baseline effects caused by strain in the glasses by averaging the positive and negative field data at a given temperature (i.e. (7 T − (−)7 T)/2). VTVH-MCD data were collected using a calibrated Cernox resistor (Lakeshore Cryogenics, calibrated 1.5–300 K) inserted into the sample cell to accurately measure the sample temperature. VTVH-MCD data were normalized to the maximum observed intensity over all isotherms for a given wavelength and the ground-state parameters were extracted by fitting in accordance with published procedures [19,20].

Computational methods. Spin unrestricted DFT calculations were performed using Gaussian 03 [21]. An experimentally calibrated user defined functional [22] (Becke's 1988 exchange functional [23] to which 10% Hartree–Fock exchange has been mixed with the correlation function of Perdew (P86) [24]) was applied as this has been found to be appropriate for evaluating O_2 reactivity which will be the subject of a future study. The triple-ζ basis set with a polarization function on heavy atoms, 6-311G*, was used to describe the Fe-atom and the delocalized π-system of the HPP and NTBC ligands, and the double-ζ basis set, 6-31G*, to describe the rest of the atoms.

The enzyme active site of HPPD was modeled using amines (NH_3) in place of histidine ligands and acetate instead of glutamate. The substrate HPP as well as the drug NTBC have been simplified by substituting the benzene ring with a methyl group. The substrate- and drug-bound complexes, both including a water molecule in the sixth coordination position, were started from the X-ray structure geometry of NTBC bound to the ferrous form of the enzyme [16]. The geometries of all species are fully optimized.

In all calculations, convergence was reached when the relative change in the density matrix between subsequent iterations was less than 1×10^{-8}. All frequencies were found to be real. The charges were calculated using Natural Population Analysis (NPA). The reported energies contain zero-point-correction energies (ZPCE). Solvation effects were included using the Polarized Continuum Model (PCM) [25–27]. The protein environment was modeled using a dielectric constant $\varepsilon = 4.0$. Molecular orbitals were analyzed using AOMix [28,29]. Orbitals were plotted using Molden [30].

The binding energies for the HPPD/Fe^{II}/NTBC and HPPD/Fe^{II}/HPP species were calculated by calculating the ΔE and ΔG between HPPD/Fe^{II}/X (X = NTBC and HPP) and X, and subsequently determining the $\Delta\Delta E$ and $\Delta\Delta G$ from these values:

$$\Delta E(\text{HPP-binding}) = E(\text{HPPD/Fe}^{II}\text{/HPP}) - E(\text{HPP})$$

$$\Delta E(\text{NTBC-binding}) = E(\text{HPPD/Fe}^{II}\text{/NTBC}) - E(\text{NTBC})$$

$$\Delta\Delta E = \Delta E(\text{HPP-binding}) - \Delta E(\text{NTBC-binding})$$

Results

CD, MCD, and VTVH-MCD of HPPD/Fe^{II}/NTBC

Near-IR (NIR) CD and MCD spectroscopy have been utilized to probe NTBC binding to HPPD/Fe^{II}. Analysis of the energies and splitting pattern of CD/MCD bands provides information about the geometric and electronic structure of NTBC bound to HPPD. In octahedral symmetry, a six-coordinate (6C) ferrous site has a doubly degenerate ^5E_g ligand-field excited state and a triply degenerate $^5T_{2g}$ ligand-field ground-state split in energy by $10\ Dq \sim 10{,}000\ cm^{-1}$ for biologically relevant nitrogen and oxygen ligands [20]. In the low symmetry of a protein active site, these states further split ($^5E_g \rightarrow d_{x^2-y^2}$ and d_z^2) resulting in two ligand-field transitions centered at $\sim$10,000 cm^{-1} and split by ~2000 cm^{-1} for a distorted 6C ferrous site. Five-coordinate (5C) square pyramidal sites show these transitions at >10,000 cm^{-1} and ~5000 cm^{-1}, and 5C trigonal bipyramidal sites exhibit one transition at <10,000 cm^{-1} and one at <5000 cm^{-1}. Distorted four-coordinate sites show only low energy ligand-field transitions in the 4000–7000 cm^{-1} region, due to the much smaller value of 10 Dq for tetrahedral complexes (10 Dq (T_d) = −4/9 10 Dq (O_h)).

While the 278 K CD spectrum of HPPD/Fe^{II} previously reported in [17] contains two broad ligand-field transitions at ~8500 and ~10,500 cm^{-1} (Fig. 2A, dashed line), addition of 2 equiv. of NTBC results in a significant change in the CD spectrum (Fig. 2A, solid line) with the presence of a negative band at ~8600 cm^{-1} and a positive band at ~11,000 cm^{-1}. The CD spectrum does not change upon further addition of NTBC, indicating complete conversion to the inhibitor bound form.

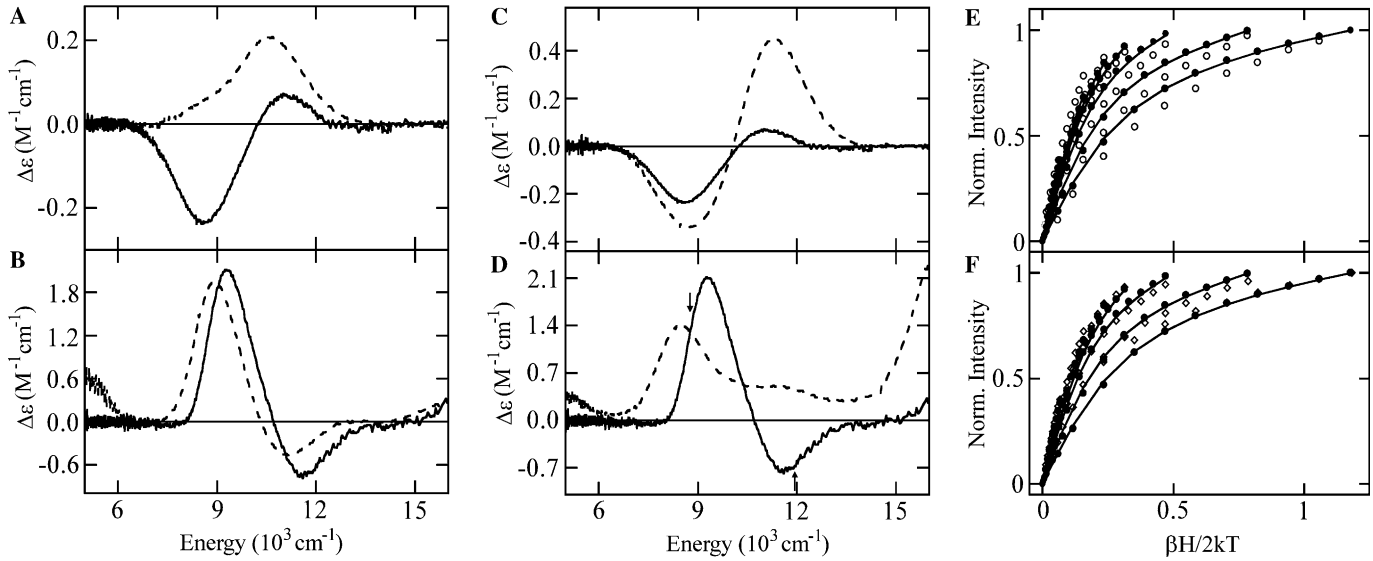

Fig. 2. NIR CD and MCD spectra of HPPD/Fe^{II}/NTBC. CD spectra at 278 K (A) and MCD spectra at 1.8 K, 7 T (B) of HPPD/Fe^{II} (dashed lines, MCD $\Delta\varepsilon \times 2$) and HPPD/$Fe^{II}$/NTBC (solid lines). CD spectra at 278 K (C) and MCD spectra at 1.8 K, 7 T (B) of HPPD/Fe^{II}/HPP (dashed lines) and HPPD/Fe^{II}/NTBC (solid lines). VTVH-MCD data (symbols) and their best fit (lines) of (E) HPPD/Fe^{II}/NTBC at 8770 cm^{-1} (●) and 11,960 cm^{-1} (○) and (F) HPPD/Fe^{II}/NTBC at 8770 cm^{-1} (●) and HPPD/Fe^{II}/HPP at 8503 cm^{-1} (◊). The arrows in (D) indicate the energy positions at which VTVH data were collected for HPPD/Fe^{II}/NTBC.

The 1.8 K, 7 T NIR MCD spectrum of HPPD/Fe^{II}/NTBC contains a positive ligand-field feature at ~9300 cm^{-1} and a negative feature at ~11,600 cm^{-1} (Fig. 2B, solid line). VTVH-MCD was used to probe the ground-state splittings of the inhibitor-bound ferrous site using the maximum of both bands to determine whether or not a mixture was present, as a single ferrous site would exhibit the same saturation behavior for both LF transitions as both derive from the same ground state (though differences in polarizations can affect this). The saturation magnetization behavior for HPPD/Fe^{II}/NTBC collected at 8770 cm^{-1} (Fig. 2E, ● symbols) is well described as a positive zero-field splitting (ZFS) non-Kramers doublet[1] (where the $M_s = 0$ sublevel of the ground state is lowest in energy) with $D = 9.8 \pm 0.3\ cm^{-1}$ and $|E| = 1.9 \pm 0.2\ cm^{-1}$, where D and E are the axial and rhombic ZFS parameters, respectively. These values correspond to $\Delta = +750 \pm 150\ cm^{-1}$ and $|V/2\Delta| = 0.24 \pm 0.2$, which reflect the axial ($E_{xz,yz} - E_{xy} = \Delta$) and rhombic ($E_{xz} - E_{yz} = V$) splitting of the $^5T_{2g}$ set of dπ orbitals on the Fe^{II}. Due to its energy position, the band at 8770 cm^{-1} could correspond to either a distorted 6C site or a trigonal bipyramidal 5C site. Since trigonal bipyramidal sites exhibit negative ZFS split ground states, this band corresponds to a 6C species. The saturation magnetization behavior at 11,960 cm^{-1} is different (Fig. 2E, ○ symbols) and cannot be fit to the same parameters. In fact, it could not be fit to any single set of spin Hamiltonian parameters, consistent with the presence of overlapping bands at this energy. Therefore, the positive and negative bands in Fig. 2D (solid line) are associated with different ferrous active sites with NTBC bound, likely a mixture of 5C and 6C species.

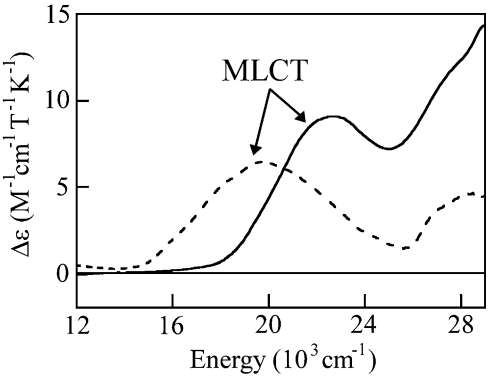

Fig. 3. UV/Vis MCD spectra of HPPD/Fe^{II}/NTBC (solid line) and HPPD/Fe^{II}/HPP (dashed line, $\Delta\varepsilon$ ($M^{-1}\ cm^{-1}\ T^{-1}\ K^{-1}$) ×2).

The $^5T_{2g}$ ground state of Fe^{II} contains the d-orbitals involved in π-bonding and backbonding. The large splitting of the ground state determined by VTVH-MCD for HPPD/Fe^{II}/NTBC is similar to that previously observed for HPPD/Fe^{II}/HPP [17], consistent with backbonding interactions between NTBC and Fe^{II}. The presence of MLCT transitions in the UV/Vis MCD spectrum of the inhibitor/drug complex (Fig. 3, solid line), where a broad positive feature at ~22,600 cm^{-1} and additional positive bands at >25,000 cm^{-1} are observed, further supports the presence of backbonding in the NTBC complex similar to that observed for bound HPP (Fig. 3, dashed line).

[1] These VTVH-MCD saturation magnetization data were fit using Eq. (1) of [19] with "δ" $= 5.2 \pm 0.2\ cm^{-1} = 2(D^2 + 3E^2)^{1/2} - D - 3E$ which is the splitting of the $M_s = 0$ and one component of the $M_s = \pm 1$ sublevels for a +ZFS-system and the polarization ratio $M_z/M_{xy} = -0.06$ for $g_\perp$ fixed at 1.0. The VTVH-MCD fit results were used to obtain $+D$ and $|E|$, and related to Δ and V as described in [20].

DFT studies of NTBC and HPP binding to HPPD/Fe^{II}

To gain further insight into the nature of the high-affinity binding of NTBC versus HPP to HPPD/Fe^{II}, DFT calculations were carried out to provide a detailed electronic description of both complexes and information on the relative binding energies of HPP and NTBC to the metal center.

Geometric structures

The geometry optimized structures of the substrate HPP and the inhibitor/drug NTBC bound to the resting ferrous active site model of the enzyme HPPD are shown in Fig. 4. Both structures are very similar and in agreement with the 2.5 Å resolution X-ray structure of ferrous HPPD/Fe^{II}/NTBC (Table 1) [16].

The substrate and the drug bind in a bidentate mode, forming a six-coordinate complex. Two amines, in place of histidine ligands, one acetate, instead of glutamate, and one water molecule complete the coordination sphere. The two oxygen atoms of the α-keto-acid ligand bound to the iron are not equivalent; the carbonyl oxygen (O_1) has a longer Fe–O and shorter C–O bond compared to the carboxylate oxygen (O_2), as is known for the bidentate ligation of α-keto acid's to metal centers [31]. The drug NTBC has a more extensive delocalized π-system, involving both oxygen atoms bound to the metal center, thus O_1 and O_2 of NTBC are equivalent, with the same Fe–O and C–O bond lengths. Despite this slight difference the geometric structures of the complexes and the binding modes of the substrate and inhibitor/drug to the metal center are very similar.

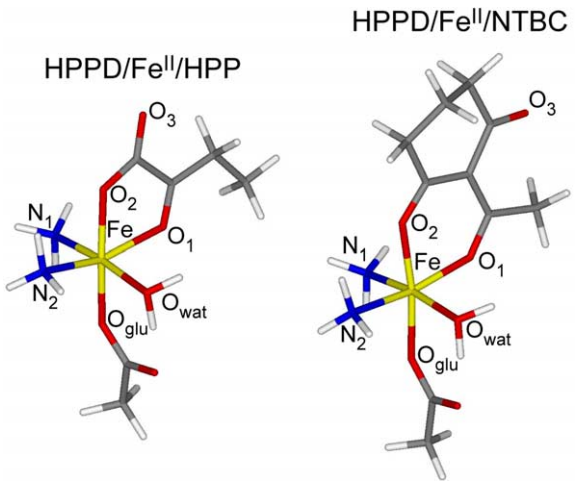

Fig. 4. Geometry optimized structures of HPPD/Fe^{II}/HPP and HPPD/Fe^{II}/NTBC.

Table 1
Structural parameters of geometry optimized HPPD/Fe^{II}/HPP and HPPD/Fe^{II}/NTBC complexes compared to the HPPD/Fe^{II}/NTBC X-ray structure

	HPPD/Fe^{II}/HPP geom-opt[a]	HPPD/Fe^{II}/NTBC geom-opt[a]	HPPD/Fe^{II}/NTBC X-ray[b]
Fe–O_1	2.14	2.01	2.03
Fe–O_2	2.04	2.04	1.93
Fe–O_{glu}	2.01	2.05	2.26
Fe–O_{wat}	2.17	2.19	2.36
Fe–N_1	2.20	2.21	2.66
Fe–N_2	2.19	2.20	2.26
O_2–Fe–O_{glu}	172	172	171
O_1–Fe–N_2	160	164	174
O_{wat}–Fe–N_1	172	171	169
O_1–Fe–O_2	77	83	81
O_1–C_1	1.24	1.27	1.39
O_2–C_2	1.29	1.27	1.23
O_{glu}–C_{glu}	1.29	1.29	1.24

[a] Optimized structures using Gaussian 03.
[b] 2.5 Å resolution X-ray [16].

Electronic structures

The structures of the free ligands HPP and NTBC, and their valence orbitals relevant for bidentate binding to the iron through the oxygen atoms O_1 and O_2 are shown in Fig. 5 (for complete energy level diagrams, see supplementary data). The HPP and NTBC π* molecular orbitals (MOs) are at low energies and unoccupied and, thus, able to interact with occupied Fe(d)-orbitals in a π-backbonding mode (due to the larger delocalized π-system of NTBC, which includes all three oxygen atoms, NTBC has two π* MOs, while HPP has only one). The energetically high

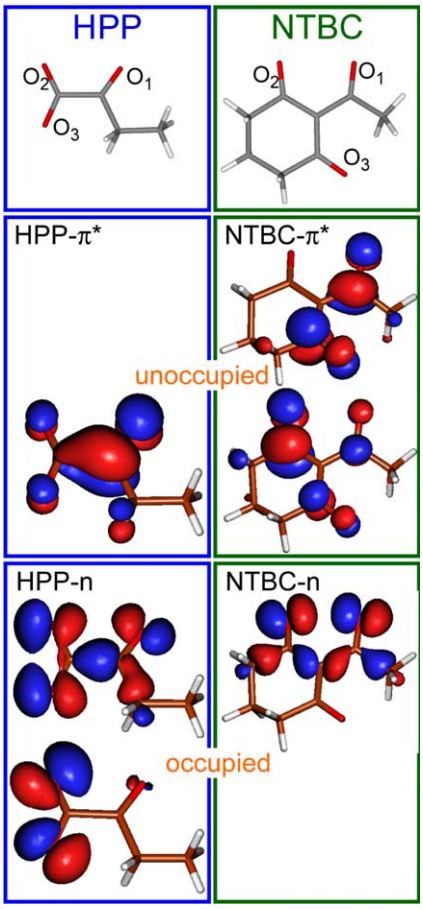

Fig. 5. Structures and relevant valence orbitals of the models of HPP and NTBC.

Table 2
Electronic structure parameters of HPPD/Fe^{II}/HPP and HPPD/Fe^{II}/NTBC

	HPPD/Fe^{II}/HPP[a]	HPPD/Fe^{II}/NTBC a
Spin densities		
Fe	3.82	3.80
O_{glu}	0.04	0.04
O_{wat}	0.03	0.03
∑(HPP/NTBC)	0.01	0.05
Charges (NPA)		
Fe	1.56	1.57
O_{glu}	−0.84	−0.84
O_{wat}	−1.03	−1.03
∑(HPP/NTBC)	0.33	0.34

[a] Fully optimized using Gaussian 03.

lying occupied "*n*" MOs can undergo σ-bonding interactions with unoccupied Fe(d)-orbitals.

Binding HPP or NTBC to the metal center results in complexes with very similar electronic structures. Both form a high-spin Fe^{II} complex ($S = 2$), with comparable spin densities and charges (Table 2). All four unpaired electrons are localized on the iron, with only small delocalization onto the ligands. The similar charge distribution in these complexes indicates comparable charge donations from the HPP/NTBC ligands to the Fe^{II} metal center and comparable backbonding of the Fe^{II} into the ligand π*.

The energy level diagrams of HPPD/Fe^{II}/HPP and HPPD/Fe^{II}/NTBC (Fig. 6) also demonstrate the similarity of both high-spin ferrous d^6 complexes (all five α-Fe(d) orbitals and one β Fe(d) orbital are occupied). In both complexes, two bonding interactions, σ-bonding and π-backbonding, between the HPP/NTBC ligand and the Fe(d) orbitals can be identified. Both are in the β-spin manifold. σ-bonding interactions between the unoccupied β-Fe(d_{z^2}) and the occupied ligand "*n*" molecular orbital (Fig. 5 and Fig. 7, top). This MO, which is mainly Fe(d_{z^2}) in character, has ~6% ligand "*n*" character due to ligand donor bonding. The occupied β-Fe(d_{xy}) orbitals form π-backbonding interactions with the low-lying unoccupied ligand π* orbitals (Fig. 7, bottom). In both complexes, about 10% of Fe(d_{xy}) is mixed in the main ligand π* MO, indicating similar π-backbonding strengths for the HPP as well as the NTBC-bound complexes. (The fact that two ligand π* MOs are available for π-backbonding interaction with the metal center in the case of NTBC does not affect the backbonding strength as the second π* MO does not participate in the bonding.) Because of the backbonding interactions in the β-spin manifold, the Fe(t_2) set (degenerate in a symmetric octahedral environment) is significantly split (Fig. 6).

The energy level diagram (Fig. 6) illustrates the nature of the lowest charge-transfer transition: it involves the excitation of a β-electron from the Fe(d_{xy}) orbital to the ligand π* orbital and is thus a metal-to-ligand charge-transfer

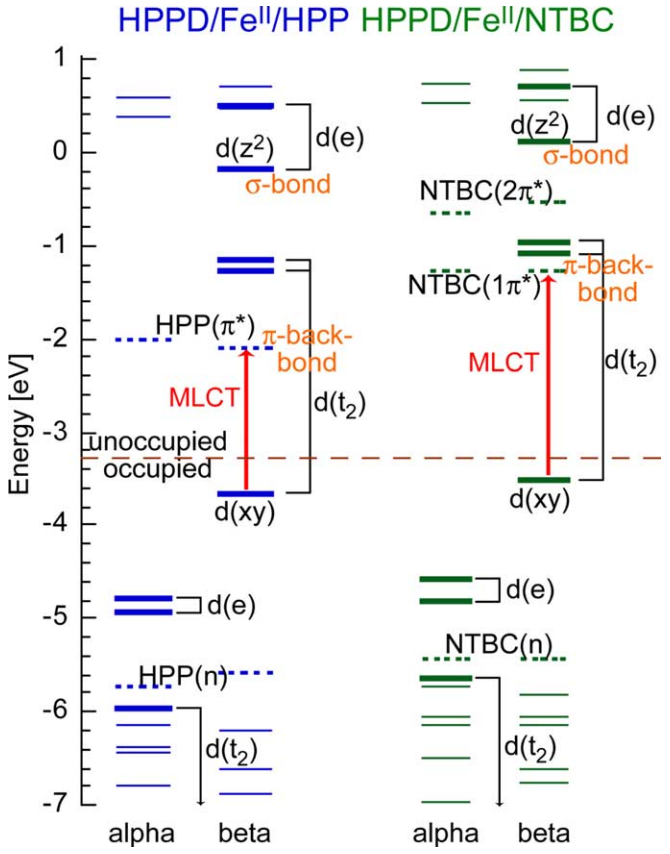

Fig. 6. Energy level diagram of HPPD/Fe^{II}/HPP and HPPD/Fe^{II}/NTBC.

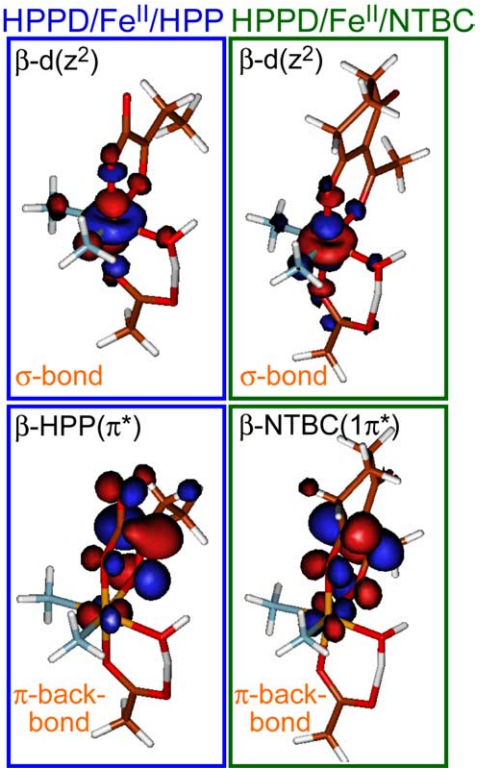

Fig. 7. Molecular orbitals showing relevant binding interactions in HPPD/Fe^{II}/HPP and HPPD/Fe^{II}/NTBC.

Table 3
Relative binding energies of HPP and NTBC to HPPD/Fe^{II}

	$\Delta\Delta E$ (gas)	$\Delta\Delta E$ (solvent)	$\Delta\Delta G$ (solvent)
HPP–NTBC	−3	−4	−3
dep. HPP–dep. NTBC	+1	+3	+3

All energies in kcal/mol; ΔE includes zero-point-correction energies, solvent: $\varepsilon = 4.0$.

(MLCT) transition. In first order, the calculations predict this MLCT transition to be at higher energy for the HPPD/Fe^{II}/NTBC complex compared to the HPPD/Fe^{II}/HPP complex. This is in agreement with the experimental observation of the MLCT transitions of the NTBC complex at higher energy than those of the HPP complex (Fig. 3).

In general, the calculations show very similar geometric and electronic structures as well as similar bonding interactions for both HPPD/Fe^{II}/HPP and HPPD/Fe^{II}/NTBC. In comparison to the MCD experiments, the calculations reproduce the π-backbonding and large Fe(t_2) energy splitting pattern.

Binding energies

Since these computational models of HPP and NTBC bound to the iron center reproduce the experimental data (backbonding, t_2-splitting, etc.), calculations were used to compare the binding energies of the substrate and the inhibitor to the iron center. The inhibitor NBTC (in its enol form, which is the predominant form at pH 7) binds less strongly to the Fe^{II} than the substrate HPP by ~3 kcal/mol (Table 3, taking solvent effects, thermal energy, and entropy effects into account).[2] If an already deprotonated ligand is bound to the metal center, the binding of NTBC is slightly favored compared to HPP by ~3 kcal/mol. Thus, the covalent binding energies for both HPP and NTBC to the Fe center are very similar, though NTBC binds slightly weaker than HPP by ~3 kcal/mol.

Discussion

The therapeutic and herbicidal properties of NTBC relate to the extremely high affinity of the molecule for the Fe^{II} site of HPPD. In this study, MCD spectroscopy and DFT calculations have been performed to elucidate the geometric and electronic structures of the drug/inhibitor complex to evaluate the contribution of bidentate coordination of NTBC to HPPD/Fe^{II} to its high affinity.

Evaluation of the MCD spectra of the NTBC-bound complex (Fig. 2D, solid line) combined with VTVH-MCD analysis indicates that HPPD/Fe^{II}/NTBC is a mixture of 5C and 6C species, where the 6C site is a significant amount of the mixture based upon the relative intensities of the corresponding transitions. By comparison, the crystallography of the NTBC complex showed the ferrous site to be predominantly composed of a 5C species, where the difference likely relates to the coordination of water which was only observed as a low occupancy ligand in one protomer of the crystal structure [16]. Analysis of the $^5T_{2g}$ ground-state splitting of the NTBC complex provides additional insight into its bonding to Fe^{II}. Since the $^5T_{2g}$ state includes the dπ-orbitals involved in π-backbonding, the large splitting determined from the VTVH-MCD data is consistent with a backbonding interaction between the bidentately coordinated NTBC and Fe^{II}. The presence of MLCT transitions in the UV/Vis MCD (Fig. 3) further supports this backbonding interaction. DFT calculations of the geometry optimized structure of HPPD/Fe^{II}/NTBC show good agreement with the geometric structure observed from crystallography, including the bidentate coordination of NTBC, bond angles, and bond lengths. The electronic structure of the complex shows the presence of π-backbonding between the occupied β-Fe(d_{xy}) orbital and the low-lying unoccupied NTBC π* orbital (Fig. 7), in agreement with the spectroscopic results.

Comparison of the spectroscopic and computational results for the NTBC complex to the complex with substrate, HPP, provides insight into potential bonding differences at the ferrous site. Previous CD and MCD studies of HPPD/Fe^{II}/HPP show similar bonding characteristics as detailed above for NTBC [17]. While the CD spectra of HPP and NTBC are nearly identical (Fig. 2C), analysis of the MCD spectrum of the HPP complex showed it also consists of a mixture of 5C and 6C species. In addition, the large $^5T_{2g}$ ground-state splitting determined from the VTVH-MCD data and the observation of MLCT transitions in the UV/Vis MCD (Fig. 3) of the HPP complex were indicative of π-backbonding between the α-keto acid moiety of HPP and Fe^{II}, analogous to the backbonding observed for the NTBC complex. Comparison of the electronic structures of the NTBC and HPP complexes shows that both of them have similar energy level diagrams (Fig. 6), where both ligands bind by σ-donation and π-backbonding. In addition, similar backbonding strengths are observed for both complexes as ~10% of Fe(d_{xy}) is mixed into the mainly ligand π* MO in both cases. Calculation of the binding energies of both NTBC and HPP showed that NTBC actually binds less strongly to Fe^{II} than HPP by ~3 kcal/mol, despite its extremely high affinity for HPPD. Therefore, the bonding description of NTBC bound to HPPD based upon the MCD and DFT studies presented herein shows that the iron coordination in both complexes is nearly identical and, thus, not solely responsible for the high affinity of the inhibitor/drug relative to substrate.

As previously mentioned, the crystallography of HPPD/Fe^{II}/NTBC identified two binding interactions of NTBC to HPPD that might relate to its high affinity: bidentate coordination to Fe^{II} and π-stacking between the aromatic ring of NTBC and two phenylalanine residues in the protein pocket (Phe364 and Phe336). Since the bonding interactions of the two complexes are very similar and NTBC actually binds more weakly to the Fe^{II} (by ~3 kcal/mol), the π-stacking interactions in the protein pocket appear

[2] The calculations reproduce correctly the experimental fact that NTBC is harder to deprotonate than HPP (experiments show a larger pK_a [15]).

to be responsible for the high-affinity binding of the drug. This could be the result of differences in the orientations of the Phe rings relative to the aromatic rings of NTBC vs. HPP or to the effects of ring substituents ($-NO_2$ and $-CF_3$ in NTBC vs. –OH in HPP), as both factors can affect the strength of π–π-stacking interactions [32].

In conclusion, we have investigated the interaction of NTBC with the ferrous active site of HPPD by MCD spectroscopy and DFT calculations to gain insight into the high affinity of this drug/inhibitor for the ferrous enzyme. Our results show a similar binding interaction and binding energy of both NTBC and substrate, HPP, to the Fe^{II} active site, indicating that the high affinity of the drug does not solely relate to its coordination. It appears that the π-stacking interactions of the aromatic rings of NTBC with aligned Phe residues in the protein pocket make a major contribution to the extremely high affinity of the drug related to its inhibition.

Acknowledgments

This research was supported by GM40392 (E.I.S), DK59551 (G.R.M.), and an NSF Graduate Fellowship to M.L.N.

Appendix A. Supplementary data

Supplementary data associated with this article can be found, in the online version, at doi:10.1016/j.bbrc.2005.08.242.

References

[1] E.I. Solomon, T.C. Brunold, M.I. Davis, J.N. Kemsley, S.-K. Lee, N. Lehnert, F. Neese, A.J. Skulan, Y.-S. Yang, J. Zhou, Geometric and electronic structure/function correlations in non-heme iron enzymes, Chem. Rev. (2000) 235–349.

[2] K. Johnson-Winters, V.M. Purpero, M. Kavana, T. Nelson, G.R. Moran, (4-Hydroxyphenyl)pyruvate dioxygenase from *Streptomyces avermitilis*: the basis for ordered substrate addition, Biochemistry 42 (2003) 2072–2080.

[3] M. Gunsior, J. Ravel, G.L. Challis, C.A. Townsend, Engineering *p*-hydroxyphenylpyruvate dioxygenase to a *p*-hydroxymandelate synthase and evidence for the proposed benzene oxide intermediate in homogentisate formation, Biochemistry 43 (2004) 663–674.

[4] R.O. Hellyer, Occurrence of beta-triketones in steam-volatile oils of some myrtaceous Australian plants, Aust. J. Chem. 21 (1968) 2825–2828.

[5] J.G. Romagni, G. Meazza, N.P.D. Nanayakkara, F.E. Dayan, The phytotoxic lichen metabolite, usnic acid, is a potent inhibitor of plant *p*-hydroxyphenylpyruvate dioxygenase, FEBS Lett. 480 (2000) 301–305.

[6] A. Schulz, O. Ort, P. Beyer, H. Kleinig, SC-0051, a 2-benzoylcyclohexane-1,3-dione bleaching herbicide, is a potent inhibitor of the enzyme *p*-hydroxyphenylpyruvate dioxygenase, FEBS Lett. 318 (1993) 162–166.

[7] J. Secor, Inhibition of barnyardgrass 4-hydroxyphenylpyruvate dioxygenase by sulcotrione, Plant Physiol. 106 (1994) 1429–1433.

[8] Y.L. Lin, C.S. Wu, S.W. Lin, D.Y. Yang, SAR studies of 2-*o*-substituted-benzoyl- and 2-alkanoylcyclohexane-1,3-diones as inhibitors of 4-hydroxyphenylpyruvate dioxygenase, Bioorg. Med. Chem. Lett. 10 (2000) 843–845.

[9] M.L. Huang, D.Y. Yang, Z.C. Shang, J.W. Zou, Q.S. Yu, 3D-QSAR studies on 4-hydroxyphenylpyruvate dioxygenase inhibitors by comparative molecular field analysis (CoMFA), Bioorg. Med. Chem. Lett. 12 (2002) 2271–2275.

[10] K.E. Pallett, S.M. Cramp, J.P. Little, P. Veerasekaran, A.J. Crudace, A.E. Slater, Isoxaflutole: the background to its discovery and the basis of its herbicidal properties, Pest Manag. Sci. 57 (2001) 133–142.

[11] G. Mitchell, D.W. Bartlett, T.E.M. Fraser, T.R. Hawkes, D.C. Holt, J.K. Townson, R.A. Wichert, Mesotrione: a new selective herbicide for use in maize, Pest Manag. Sci. 57 (2001) 120–128.

[12] S. Lindstedt, E. Holme, E.A. Lock, O. Hjalmarson, B. Strandvik, Treatment of hereditary tyrosinemia type-I by inhibition of 4-hydroxyphenylpyruvate dioxygenase, Lancet 340 (1992) 813–817.

[13] E. Holme, S. Lindstedt, Tyrosinaemia type I and NTBC (2-(2-nitro-4-trifluoromethylbenzoyl)-1,3-cyclohexanedione), J. Inherit. Metab. Dis. 21 (1998) 507–517.

[14] C. Phornphutkul, W.J. Introne, M.B. Perry, I. Bernardini, M.D. Murphey, D.L. Fitzpatrick, P.D. Andersen, M. Huizing, Y. Anikster, L.H. Gerber, W.A. Gahl, Natural history of alkaptonuria, N. Engl. J. Med. 347 (2002) 2111–2121.

[15] M. Kavana, G.R. Moran, Interaction of (4-hydroxyphenyl)pyruvate dioxygenase with the specific inhibitor 2-[2-nitro-4-(trifluoromethyl)benzoyl]-1,3-cyclohexanedione, Biochemistry 42 (2003) 10238–10245.

[16] J.M. Brownlee, K. Johnson-Winters, D.H.T. Harrison, G.R. Moran, Structure of the ferrous form of (4-hydroxyphenyl)pyruvate dioxygenase from *Streptomyces avermitilis* in complex with the therapeutic herbicide, NTBC, Biochemistry 43 (2004) 6370–6377.

[17] M.L. Neidig, M. Kavana, G.R. Moran, E.I. Solomon, CD and MCD studies of the non-heme ferrous active site in (4-hydroxyphenyl)pyruvate dioxygenase: correlation between oxygen activation in the extradiol and alpha-KG-dependent dioxygenases, J. Am. Chem. Soc. 126 (2004) 4486–4487.

[18] M.I. Davis, E.C. Wasinger, A. Decker, M.Y.M. Pau, F.H. Vaillancourt, J.T. Bolin, L.D. Eltis, B. Hedman, K.O. Hodgson, E.I. Solomon, Spectroscopic and electronic structure studies of 2,3-dihydroxybiphenyl 1,2-dioxygenase: O-2 reactivity of the non-heme ferrous site in extradiol dioxygenases, J. Am. Chem. Soc. 125 (2003) 11214–11227.

[19] E.G. Pavel, N. Kitajima, E.I. Solomon, Magnetic circular dichroism spectroscopic studies of mononuclear non-heme ferrous model complexes: correlation of excited state and ground state electronic structure with geometry, J. Am. Chem. Soc. 120 (1998) 3949–3962.

[20] E.I. Solomon, E.G. Pavel, K.E. Loeb, C. Campochiaro, Magnetic circular dichroism spectroscopy as a probe of the geometric and electronic structure of non-heme ferrous enzymes, Coord. Chem. Rev. 144 (1995) 369–460.

[21] R.C. Gaussian 03, M.J. Frisch, G.W. Trucks, H.B. Schlegel, G.E. Scuseria, M.A. Robb, J.R. Cheeseman, J.A. Montgomery, Jr., T. Vreven, K.N. Kudin, J.C. Burant, J.M. Millam, S.S. Iyengar, J. Tomasi, V. Barone, B. Mennucci, M. Cossi, G. Scalmani, N. Rega, G.A. Petersson, H. Nakatsuji, M. Hada, M. Ehara, K. Toyota, R. Fukuda, J. Hasegawa, M. Ishida, T. Nakajima, Y. Honda, O. Kitao, H. Nakai, M. Klene, X. Li, J.E. Knox, H.P. Hratchian, J.B. Cross, V. Bakken, C. Adamo, J. Jaramillo, R. Gomperts, R.E. Stratmann, O. Yazyev, A.J. Austin, R. Cammi, C. Pomelli, J.W. Ochterski, P.Y. Ayala, K. Morokuma, G.A. Voth, P. Salvador, J.J. Dannenberg, V.G. Zakrzewski, S. Dapprich, A.D. Daniels, M.C. Strain, O. Farkas, D.K. Malick, A.D. Rabuck, K. Raghavachari, J.B. Foresman, J.V. Ortiz, Q. Cui, A.G. Baboul, S. Clifford, J. Cioslowski, B.B. Stefanov, G. Liu, A. Liashenko, P. Piskorz, I. Komaromi, R.L. Martin, D.J. Fox, T. Keith, M.A. Al-Laham, C.Y. Peng, A. Nanayakkara, M. Challacombe, P.M.W. Gill, B. Johnson, W. Chen, M.W. Wong, C. Gonzalez, J.A. Pople, Gaussian, Inc., Wallingford, CT, 2004.

[22] G. Schenk, M.Y.M. Pau, E.I. Solomon, Comparison between the geometric and electronic structures and reactivities of (FeNO)7 and (FeO2)8 complexes: a density functional theory study, J. Am. Chem. Soc. 126 (2004) 505–515.

[23] A.D. Becke, Density-functional exchange-energy approximation with correct asymptotic-behavior, Phys. Rev. A 38 (1988) 3098–3100.

[24] J.P. Perdew, Density-functional approximation for the correlation energy of the inhomogeneous electron gas, Phys. Rev. B 33 (1986) 8822–8824.
[25] E. Cances, B. Mennucci, J. Tomasi, A new integral equation formalism for the polarizable continuum model: theoretical background and applications to isotropic and anisotropic dielectrics, J. Chem. Phys. 107 (1997) 3032–3041.
[26] M. Cossi, V. Barone, B. Mennucci, J. Tomasi, Ab initio study of ionic solutions by a polarizable continuum dielectric model, Chem. Phys. Lett. 286 (1998) 253–260.
[27] B. Mennucci, J. Tomasi, Continuum solvation models: a new approach to the problem of solute's charge distribution and cavity boundaries, J. Chem. Phys. 106 (1997) 5151–5158.
[28] S.I. Gorelsky, AOMix program, rev. 6.04, http://www.sg-chem.net/.
[29] S.I. Gorelsky, A.B.P. Lever, Electronic structure and spectra of ruthenium diimine complexes by density functional theory and INDO/S. Comparison of the two methods, J. Organomet. Chem. 635 (2001) 187–196.
[30] G. Schaftenaar, J.H. Noordik, Molden: a pre- and post-processing program for molecular and electronic structures, J. Comput.-Aid. Mol. Des. 14 (2000) 123–134, <http://www.cmbi.ru.nl/molden/molden.html>.
[31] Z.H. Zhang, J.S. Ren, D.K. Stammers, J.E. Baldwin, K. Harlos, C.J. Schofield, Structural origins of the selectivity of the trifunctional oxygenase clavaminic acid synthase, Nat. Struct. Biol. 7 (2000) 127–133.
[32] C.A. Hunter, J.K.M. Sanders, The nature of pi–pi interactions, J. Am. Chem. Soc. 112 (1990) 5525–5534.